

# Effect of Grid Resolution on the Simulation of Perched Water Zones

Zhiming Lu and Bruce A. Robinson

Hydrology, Geochemistry, and Geology Group  
Los Alamos National Laboratory

September 29, 2006

Submitted to LANL Groundwater Protection Program to fulfill FY06  
Vadose Zone Project deliverable

## 1. Introduction

Deep perched groundwater occurs at widely dispersed locations across the Pajarito Plateau. Robinson et al. (2005) investigated the perched-zone occurrences at the Pajarito Plateau. Their study identified a total of 33 perched-zone occurrences in 29 wells. The saturated thickness of perched zones is highly variable, ranging from about 1 to 122 m (400 ft). Deep perched groundwater is most often found beneath wet canyons, suggesting that in addition to perching horizons, locally high percolation rates are required to yield saturated conditions.

Robinson et al. (2005) developed a model for simulating deep perched groundwater in vadose zone. The model considers the *interfaces* between hydrogeologic units to be the horizons where the saturated permeability is lower than either of the units above or below the interface. A constant multiplier called the permeability reduction factor is applied at the interface between two hydrostratigraphic units to simulate the perching horizon. It has been demonstrated in two-dimensional numerical simulations at Los Alamos Canyon that simulated results replicate perched saturation as observed.

In this study, we investigate how the vertical grid resolution in the area right above the interfaces will affect the formation of perching water zones. The hydraulics of a combined unsaturated and saturated flow domain is highly nonlinear, and perched-water zones are often thin, leading us to question the validity of perched water simulations in large-scale models, which necessarily employ fairly coarse grids. In addition, we examine the effect of the net infiltration rate on development of these perching zones.

## 2. Flow Simulations

### 2.1. Flow model.

We consider transient flow in variably saturated porous media satisfying the following continuity equation and Darcy's law:

$$-\nabla \cdot \mathbf{q}(\mathbf{x}, t) + g(\mathbf{x}, t) = C_s(\psi) \frac{\partial \psi(\mathbf{x}, t)}{\partial t}, \quad (1)$$

$$\mathbf{q}(\mathbf{x}, t) = -K[\psi] \nabla[\psi(\mathbf{x}, t) + x_1], \quad (2)$$

subject to initial and boundary conditions

$$\psi(\mathbf{x}, 0) = \Psi_0(\mathbf{x}), \quad \mathbf{x} \in \Omega, \quad (3)$$

$$\psi(\mathbf{x}, t) = \Psi(\mathbf{x}, t), \quad \mathbf{x} \in \Gamma_D \quad (4)$$

$$\mathbf{q}(\mathbf{x}, t) \cdot \mathbf{n}(\mathbf{x}) = Q(\mathbf{x}, t), \quad \mathbf{x} \in \Gamma_N, \quad (5)$$

where  $\mathbf{q}$  is the specific discharge (flux),  $\psi(\mathbf{x}, t) + x_1$  is the total head,  $\psi$  is the pressure head,  $\Psi_0(\mathbf{x})$  is the initial pressure head in the domain  $\Omega$ ,  $\Psi(\mathbf{x}, t)$  is the prescribed head on Dirichlet boundary segments  $\Gamma_D$ ,  $Q(\mathbf{x}, t)$  is the prescribed flux

across Neumann boundary segments  $\Gamma_N$ ,  $\mathbf{n}(\mathbf{x})=(n_1, \dots, n_d)^T$  is an outward unit vector normal to the boundary,  $C[\psi]=d\theta/d\psi$  is the specific moisture capacity,  $\theta$  is the volumetric water content, and  $K[\psi]$  is the unsaturated hydraulic conductivity (assumed to be isotropic locally). Both  $C$  and  $K$  are functions of pressure head and soil properties at  $\mathbf{x}$ . For convenience, they will be written as  $C(\mathbf{x},t)$  and  $K(\mathbf{x},t)$  in the sequel. The elevation  $x_1$  is directed vertically upward. In these coordinates, recharge has a negative sign.

It is clear that models are needed to describe the constitutive relationships between  $K$ s versus  $\psi$  and  $\theta_e$  versus  $\psi$  when the flow is unsaturated. In this study, we use the van Genuchten-Mualem model:

$$K(\mathbf{x},t) = K_s(\mathbf{x})\sqrt{S(\mathbf{x},t)}\{1 - [1 - S^{1/m}(\mathbf{x},t)]^m\}^2 \quad (6)$$

$$S(\mathbf{x},t) = \{1 + [-\alpha(\mathbf{x})\psi(\mathbf{x},t)]^n\}^{-m}, \quad (7)$$

where  $\psi \leq 0$ . In the above,  $S(\mathbf{x},t) = \theta_e/(\theta_s - \theta_r)$  is the effective saturation,  $\theta_r$  is the residual (irreducible) water content,  $\theta_s$  is the saturated water content,  $\alpha$  is the pore-size distribution parameter, and  $n$  is a fitting parameter, and  $m = 1 - 1/n$ .

## 2.2. Simulation domain and numerical grid

In this study, we perform idealized, two-dimensional simulations along the direction of a sloping perched zone, perhaps along the axis of a canyon such as Los Alamos or Mortendad Canyons. For this, we consider a two-dimensional cross section of size  $5000\text{m} \times 200\text{m}$ , discretized into rectangular elements of  $20\text{m} \times 10\text{m}$  for the area  $x = -500 \sim 500\text{m}$  and  $y = 0 \sim 200$  (the center part) and  $200\text{m} \times 10\text{m}$  for the rest of the domain (Figure 2.1a). The generated grid is then rotated 3 degrees (about 5.2% of slope) clockwise around the fixed reference location (0,0), which yields the grid as shown in Figure 2.1b. Note that each element in the new grid is still rectangular, although they look distorted because of the vertical exaggeration in this plot. An area of  $5000\text{m} \times 30\text{m}$ ,  $x = -2500\text{m} \sim 2500\text{m}$  and  $y = 100\text{m} \sim 130\text{m}$ , will be refined with different vertical resolutions, and the effect of vertical grid resolution in this area on flow and transport behaviors will be explored.

## 2.3. Boundary conditions

The boundary conditions for the flow simulation are: water infiltration at the top, water table at the bottom, and non-flow at two lateral boundaries. The magnitude of the net infiltration rate varies for different cases.

## 2.4. Model parameters

FEHM is the numerical model used to perform the model runs. The hydraulic properties are chosen to be those of the Otowi member of Bandelier Tuff (Qbof). The soil parameters for this unit are taken from the previous reports:

$$\text{Permeability } k = 7.25 \times 10^{-13} \text{ m}^2,$$

Pore-size distribution parameter  $\alpha = 0.66 \text{ m}^{-1}$ ,  
van Genuchten fitting parameter  $n = 1.711$ ,  
Porosity  $\phi = 0.469$ ,  
Rock density  $= 1180 \text{ kg/m}^3$ , and  
Residual water content  $\theta_r = 0.026$ .

These properties are the same for both zones. FEHM's ITFC macro that defines flow and transport parameters at interfaces between pairs of zones is used and the permeability reduction factor is chosen to be  $2 \times 10^{-4}$ , which means that the harmonically weighted saturated permeability is multiplied by this number for all connections at the interfaces between zones 1 and 2.

## 2.5. Steady state modeling

To investigate the effect of grid resolutions on the formation of perched water zone, we ran a series of steady state modeling with different vertical grid resolutions in the area right above the interface between two zones. The effect of the net infiltration rate on the perching zone is also investigated by using three different rates, the base case infiltration rate of  $q = 150 \text{ mm/yr}$ , a relative lower rate of  $50 \text{ mm/yr}$ , and a higher rate of  $250 \text{ mm/yr}$ .

*2.5.1. Base case infiltration rate.* Figures 2.3 and 2.4 illustrate the saturation distribution and the pressure head at steady state for different grid resolutions for the base case simulation (a net infiltration rate of  $150 \text{ mm/yr}$ ). Also illustrated in the figures are three streamlines for each case. Note that at relatively coarse grids the fluid moves towards the interface and then tends to pass through the interface.

In all these cases, a perched water zone is formed above the interface. The perched water zone is defined as the collection of those grid nodes (and volumes associated with these nodes) with positive pressure head and saturation  $S = 1$ . We calculated both the average thickness and average length of the perched zone for each case. Figure 2.5 shows that there is a large variation on the average length at low vertical resolution, and as the resolution increases the average length becomes stabilized. This figure also indicates that the grid resolution may have a significant effect on the perched zone thickness. At the coarsest grid ( $\Delta y = 10 \text{ m}$ ), the average thickness is  $10 \text{ m}$ , which means that only one layer of grid nodes are saturated above the interface. As the grid becomes finer, there is only a slight increase in saturated thickness until the grid resolution becomes very small. In both cases of  $\Delta y = 0.25 \text{ m}$  and  $\Delta y = 0.1 \text{ m}$ , the average thickness of the perching zone is nearly doubled.

The average horizontal velocity component and maximum horizontal velocity component computed from the entire perched zone are illustrated in Figure 2.6. The figure shows that both the average horizontal velocity and the maximum horizontal velocity increase as the grid becomes finer. Since the state variables (pressure head and velocity fields) at any node represent the averaged quantities over the volume associated with the node, the spatial variability of state variables are smoothed out at low grid resolutions.

To examine the velocity component at more detail, we compare the distribution of the velocity fields in the perched zone for two grid resolutions  $\Delta y = 10\text{m}$  and  $\Delta y = 0.25\text{m}$ , as illustrated in Figures 2.7 and 2.8 for both the horizontal and vertical velocity components. It is seen from Figure 2.7 that in most area of perching zone the horizontal velocity component is greater than  $0.05\text{m/day}$  for the case with  $\Delta y = 0.25\text{m}$  (Fig 2.7b), while at the coarse grid of  $\Delta y = 10\text{m}$ , the horizontal velocity component is almost always less than  $0.05\text{m/day}$  (Fig. 2.7a). The vertical velocity components for two different grid resolutions are compared in Figure 2.8. The figure clearly indicates that there may have some numerical instability when the grid is too coarse.

**2.5.2 Higher infiltration rate.** For a relatively high infiltration rate of  $250\text{mm/yr}$ , similar numerical experiments are conducted and results are illustrated in Figures 2.9--2.11. Compared to the base case simulations, the effect of grid resolution on the size of the perched water zone is less significant, but still present. At large grid sizes, there are some variations on the average length and the average thickness, but both quickly become stabilized as the grid resolution increases. For the coarse grid, it seems that the perched zone is more uniformly distributed along the interface. As the resolution increases, the perched zone becomes lens-shaped, with a larger thickness toward the center of the domain. Again, the average velocity and the maximum velocity of the perched zone increase with increase of the grid resolution.

**2.5.3 Lower infiltration rate.** We conduct a set of numerical simulations with different vertical resolutions,  $10\text{m}$ ,  $5\text{m}$ ,  $2\text{m}$ ,  $1\text{m}$ ,  $0.5\text{m}$ , and  $0.25\text{m}$ , under a relatively low infiltration rate of  $50\text{mm/yr}$ . The distribution of steady-state water saturation for different vertical resolutions at this low infiltration rate is depicted in Figure 2.12. The numerical results indicate that perching zone occurs only at the smallest grid resolution of  $\Delta y = 0.25\text{m}$  and all other coarser grid simulations cannot capture the perching zone. For the case of  $\Delta y = 0.25\text{m}$ , the average length and average thickness of the perched water zone is  $1472\text{m}$  and  $8.4\text{m}$ , respectively. It is interesting to note that several vertical grid resolutions ( $5\text{m}$ ,  $2\text{m}$ ,  $1\text{m}$ , and  $0.5\text{m}$ ) used for this set of simulations are smaller than the average thickness of the perched water zone ( $8.4\text{m}$ ), but simulations with these grids cannot reproduce the perched water zone.

## **2.6. Transient Simulation.**

To explore the transient behavior of perched zone development, we ran three numerical simulations. In the first two simulations, we examine the effect of grid resolution on the development of perched water zone. The vertical grid resolutions used for this purpose are  $\Delta y = 10\text{m}$  and  $\Delta y = 1\text{m}$  in the region  $x = -2500 \sim 2500$  and  $y = 100 \sim 130\text{m}$ . For both grids, we first ran a steady state simulation under the given grid with an infiltration rate of  $10\text{mm/year}$  at the entire top boundary and took this steady state flow field as the initial condition for the transient runs. In transient simulations, the infiltration rate is changed to  $1000\text{mm/year}$  in the segment  $x = -500 \sim 500\text{m}$  of the top boundary while the rate at the

rest of top boundary is kept the same as in the steady state simulation. The results for two different cases are illustrated in Figures 2.13--2.18.

The saturation distribution at a few selected elapsed times for the case with the grid resolution of  $\Delta y = 10\text{m}$  is shown in Figure 2.13. The figure clearly shows the development of the perched water zone over time. Initially, because of the small infiltration (10mm/yr), there is no perched zone at all. Due to increased infiltration in the center segment of the top boundary at time  $t = 0$ , the water moves downward and accumulates right above the interface after 15 years, and the average length and average thickness of the perched water zone tends to increase with the time (Figure 2.14). Both the average velocity and the maximum velocity of in the perched water zone all increase with time (Figure 2.15). The flow system reaches the steady state after about 50 years. This time will depend on the specific infiltration rate scenario assumed.

Figures 2.16—2.18 convey similar information for the case of grid resolution  $\Delta y = 1\text{m}$ . Compared to Figure 2.13, it is seen that, with a coarser grid, the water moves fast in the upper portion of the unsaturated domain because of numerical dispersion (Fig. 2.13). However, the perched water zone is developed earlier when the grid is finer, because it takes much more time to form a perched water layer of 10m in thickness in the coarser grid of  $\Delta y = 10\text{m}$ . While the perched water zone appears to be terraced at  $\Delta y = 10\text{m}$ , it becomes a smooth, lens-shaped zone at  $\Delta y = 1\text{m}$ . In addition, it seems that the average thickness from the simulation with  $\Delta y = 1\text{m}$  is slightly larger than that for the case with  $\Delta y = 10\text{m}$ , while the average length is reversed.

### 3. Numerical Transport Simulations

#### 3.1. Transport Model

The transport of a nonreactive solute can be described by recording the position of a particle at time  $t$  that originates from position  $\mathbf{a}$  at time  $t = t_0$

$$\frac{d\mathbf{X}(t;\mathbf{a})}{dt} = \mathbf{V}(\mathbf{X}), \quad (8)$$

with the initial condition of  $\mathbf{X}(t_0;\mathbf{a}) = \mathbf{a}$ , where  $\mathbf{V}$  is Lagrangian velocity. Here  $\mathbf{X} = (\mathbf{X}_1, \mathbf{X}_2, \mathbf{X}_3)$  is the location of the particle at time  $t$ . The Eulerian velocity field is obtained from steady-state flow simulations using FEHM as described previously and converted to Lagrangian velocity. Equation (8) is solved numerically using the fourth-order RK method and the particle's position at any time  $t$  is recorded. Based on these records, the travel time for the particle along its streamline can also be determined.

Three particles are released at locations  $(-1000\text{m}, 240\text{m})$ ,  $(0\text{m}, 180\text{m})$ , and  $(1000\text{m}, 140\text{m})$ , respectively, into the steady state flow fields as presented in Section 2.5. A particle tracking method based on integration of equation (8) by the fourth-order Runge-Kutta method is used to find the particles' positions at any time (Lu and Zhang, 2003). Both travel time and the particles' positions will be

compared for different vertical grid resolutions and different strength of the infiltration at the top boundary.

### 3.2. Simulation Results

The particle positions at certain elapsed times for the fixed grid resolution  $\Delta y = 0.5\text{m}$  but varying infiltration rates are plotted in Figures 3.1—3.3, where circles in these figures represent particle's positions along their paths at different times (200 days between two adjacent circles in Figures 3.1—3.2, and 1000 days in Figure 3.3). The distance between any two consecutive points is an indication of the particle's local travel velocity. The total travel time, the time required for a released particle to exit the system, as a function of infiltration rate is depicted in Figure 3.4 for both grid resolution  $\Delta y = 0.5\text{m}$  and  $10\text{m}$ .

Several observations can be made from these figures. First, particles move much faster in the perched water zone than in the unsaturated media, which is expected as the travel velocity in the saturated perching zone is in general larger than that in unsaturated zone. In particular, the total travel time for the third particle to exit the system is relatively large even though its travel distance is smallest, because the third particle travels only in the unsaturated zone. Second, the total travel time heavily depends on the infiltration rate (Figure 3.4). It should be noted that the travel time is not proportional to the infiltration rate, because of the nonlinear nature of the unsaturated flow. Third, the elevation at which a particle exits the system also depends on the infiltration rate; the lower the infiltration rate, the higher the exiting elevation. In fact, the particles' exiting elevations for three different infiltration rates of  $50\text{mm/yr}$ ,  $150\text{mm/yr}$ , and  $250\text{mm/yr}$  are  $-106\text{m}$ ,  $-108\text{m}$ , and  $-120\text{m}$ , respectively, for both grid resolutions.

Figures 3.5—3.7 illustrate the components of particles' trajectories,  $\mathbf{X}_1$  and  $\mathbf{X}_2$ , at the base case infiltration rate for different grid resolutions. The slopes of curves in these diagrams represent the travel velocity components. It is seen that the grid resolution does not have an important effect on the travel time for particle 3 (Fig. 3.7), which is located in downstream of perching zones.

However, these figures reveal that the vertical resolution may have a significant impact on the travel time for other two particles. For example, for the first particle (P1), although at the early time ( $<1750$  days, see Fig. 3.4) it moves only downwards regardless the grid resolution, it then quickly moves to the interface just in a few hundred days in fine-grid simulations, while it takes an additional 3000 days to reach the interface for the grid resolution  $\Delta y = 10\text{m}$ . In general, these particles travel much faster within the perched zones in finer grids than in coarser grids. The figure also shows that at the later time the particle moves in a similar way for all grid resolutions, as demonstrated by the similar pattern. The total travel time for particle P1 can range from about 5000 days to nearly 8000 days, yielding a relative error of about 60%. If the particle was originally located at, for example,  $(-1000\text{m}, 170\text{m})$ , the total travel time would range from about 3000 days to 6000 days, which gives a relative error of about 100%.

The importance of such impact depends on the strength of the infiltration rate. When the infiltration rate is high, as demonstrated in Figures 3.8--3.10, the relative difference of the total travel time between different vertical resolutions can be very large. Figure 3.8 shows that the total travel time for particle P1 ranges from 2000 days to 6000 days, a relative error of about 200%. It seems that this contradicts to the previous observation (Section 2.5.2) that at large infiltration rates the grid resolution does not have a significant impact on the perched water zones. This may be explained by examining the velocity fields at detail, as displayed in Figures 3.11-3.12. These figures show that the velocity components are larger when the grid resolution is high. More importantly, both particles P1 and P2 travel along the fast path for  $\Delta y = 0.25\text{m}$ . For  $\Delta y = 10\text{m}$ , the particles move even upward in some portions because of the upward vertical velocity components. For the low infiltration rate (Figs. 3.13--3.15), the relative difference can be as large as three times, although the absolute difference of the total travel time can be very large.

#### **4. Conclusions and Discussion**

In this study, we investigated the effect of the vertical grid resolution on the simulation of perched water zones using two-dimensional examples, where the hydraulic properties are chosen to be those of the Otowi member of Bandelier Tuff (Qbof). The dependence of the perched water zone on the net infiltration rate is also explored. The following conclusions can be drawn from this study

1. The vertical grid resolution has a significant impact on the simulation of the perched water zones. The average thickness and average length of the perching zones vary with the grid resolution. In some cases, simulations with low grid resolutions may not capture perching zones, especially when the infiltration rate is low. In the area with a low infiltration rate, the grid size should be much smaller so that possible perching zones may be captured.
2. Since velocity fields vary dramatically with the grid resolution, the effect of the grid resolution on solute transport is more significant than on development of perching zones. The relative error of the total travel time for a particle to exit the system computed from different grid resolutions can be as large as 200% under some circumstances.

The implications of these results on future vadose zone modeling on the Pajarito Plateau are profound. Accuracy and reliability of numerical model results are critical to studies that use simulation to predict the movement of water and contaminants through the vadose zone. Perched water zones are often pointed to as evidence of potential fast pathways for contaminants to the water table. The predicted velocity of migration, and the lateral displacements of contaminants away from their source locations at the surface are shown to be susceptible to grid resolution effects. Large-scale, three-dimensional models of canyons typical have grids with vertical resolutions on the high end of those studied here. However, this study shows that this resolution is inadequate to reach convergence to a stable solution to the perched water problem, for either the velocities in the zone, or



even the thickness of the zone. A factor of one hundred reduction in grid spacing is shown to be needed in some cases, a result that implies that using current computational approaches, simulated perched zones are not reliable for predictive purposes.

It might be argued that through calibration to observed thicknesses of perched zones, one can reproduce perched water in a reasonable way in large-scale models. If the modeling goal is to predict perched thickness, or to reproduce the locations of perched zone across a large model domain, this argument is probably valid, although it would need to be argued that known numerical inaccuracies do not influence any conclusions. However, if the goal is to predict transport velocity, typical grid resolutions are simply insufficient for this modeling problem. Ad hoc corrections to model properties or simulation results are one approach to correcting this problem. In the longer term, new numerical methods are required to tackle this issue in a scientifically robust way. Possible approaches include: 1) use of new analytical solutions for phreatic flow within a large scale computational model; 2) development of adaptive grid methods to refine the grid locally and “on the fly” to provide the needed resolution at an acceptable computational cost; 3) embed new computational approaches suited for tracking interfaces, such as smooth particle hydrodynamics, within our current numerical framework to locally provide accurate simulations. These options are long-term solutions to the problem, and would require extensive research to implement.

## **5. Acknowledgement**

The authors thank George Zyvoloski and Kay Birdsell for useful technical discussions regarding this simulation problem.

## **6. References**

- Birdsell, K. H., B. D. Newman, D. E. Broxton, and B. A. Robinson, 2005, this issue. Conceptual models of vadose-zone flow and transport beneath the Pajarito Plateau, Los Alamos, New Mexico. *Vadose Zone J.*
- Carrera, J., and S. P. Neuman, Estimation of aquifer parameters under transient and steady state conditions, 1. Maximum likelihood method incorporating prior information, *Water Resour. Res.*, 22(2), 199-210, 1986.
- Clifton, P. M., and S. P. Neuman, Effects of kriging and inverse modeling on conditional simulation of the Avra Valley aquifer in southern Arizona, *Water Resour. Res.*, 18(4), 1215-1234, 1982.
- Dander, D. C., 1998. Unsaturated groundwater flow beneath upper Mortandad Canyon, Los Alamos, New Mexico, Los Alamos National Laboratory report LA-UR-98-4759, Los Alamos, New Mexico.
- Kwicklis, E., M. Witkowski, K. Birdsell, B. Newman, and D. Walther, 2005. Development of an infiltration map for the Los Alamos area, New Mexico, *Vadose Zone J.*, 4, 672-693.

- Lu, Z. , and D. Zhang, Solute spreading in nonstationary flows in bounded heterogeneous saturated-unsaturated media, *Water Resour. Res.*, 39(3), 1049, doi:10.1029/ 2001WR000908, 2003.
- Bobinson, B., D. Broxton, and D. Vaniman, Observations and modeling of deep perched water beneath the Pajarito Plateau, *Vadose Zone J.* doi:10.2136/vzj/2004.0168, 4, 637-652, 2005.
- Rogers, D. B., and B. M.Gallaher, 1995. The Unsaturated hydraulic characteristics of the Bandelier Tuff, Los Alamos National Laboratory report LA-12968-MS, Los Alamos, New Mexico.
- Rogers, D.B., B.M. Gallaher and E.L. Vold, 1996. Vadose zone infiltration beneath the Pajarito Plateau at Los Alamos National Laboratory,” New Mexico Geological Society Guidebook, 47<sup>th</sup> Field Conference, Jemez Mountains Region, pp. 413-420.
- van Genuchten, M. T., 1980. A closed-form equation for predicting the hydraulic conductivity of unsaturated soils, *Soil Sci. Soc. Amer. J.*, 44 892- 898.
- Zyvoloski, G.A., B.A. Robinson, Z.V. Dash, and L.L. Trease, 1997. Summary of the models and methods for the FEHM application - A finite-element heat-and mass-transfer code. Report LA-13307-MS, Los Alamos National Laboratory, Los Alamos, New Mexico.

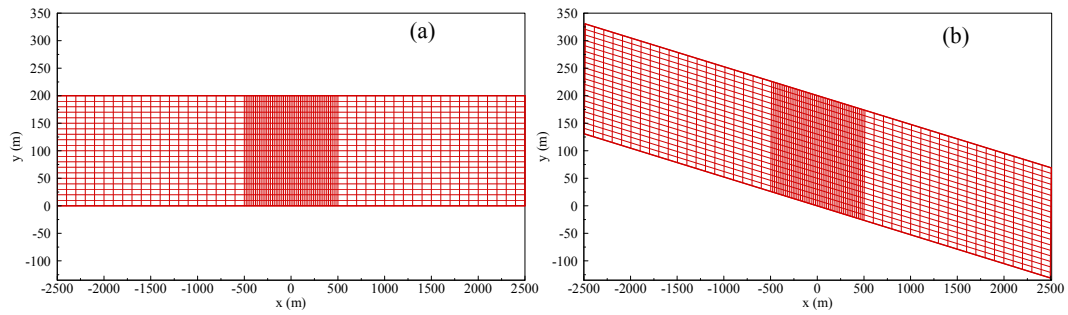


Figure 2.1: (a) Simulation domain and grid before rotation, and (b) the actual grid used in simulation.

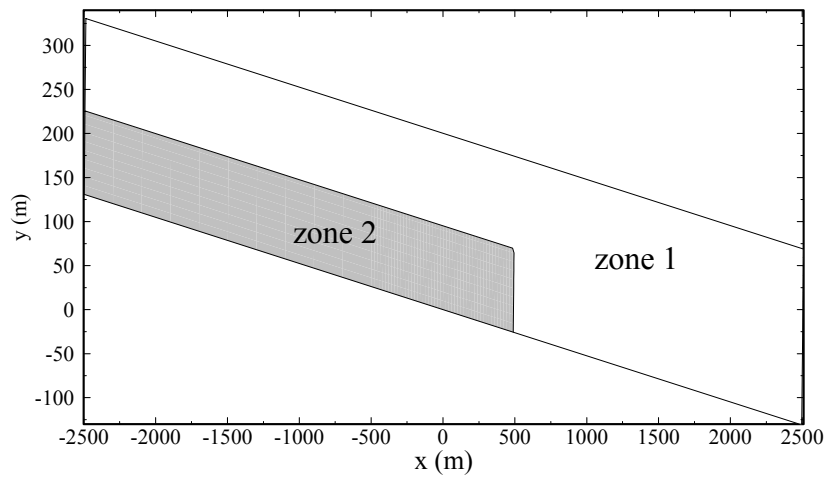


Figure 2.2. The simulation domain is divided into 2 zones.

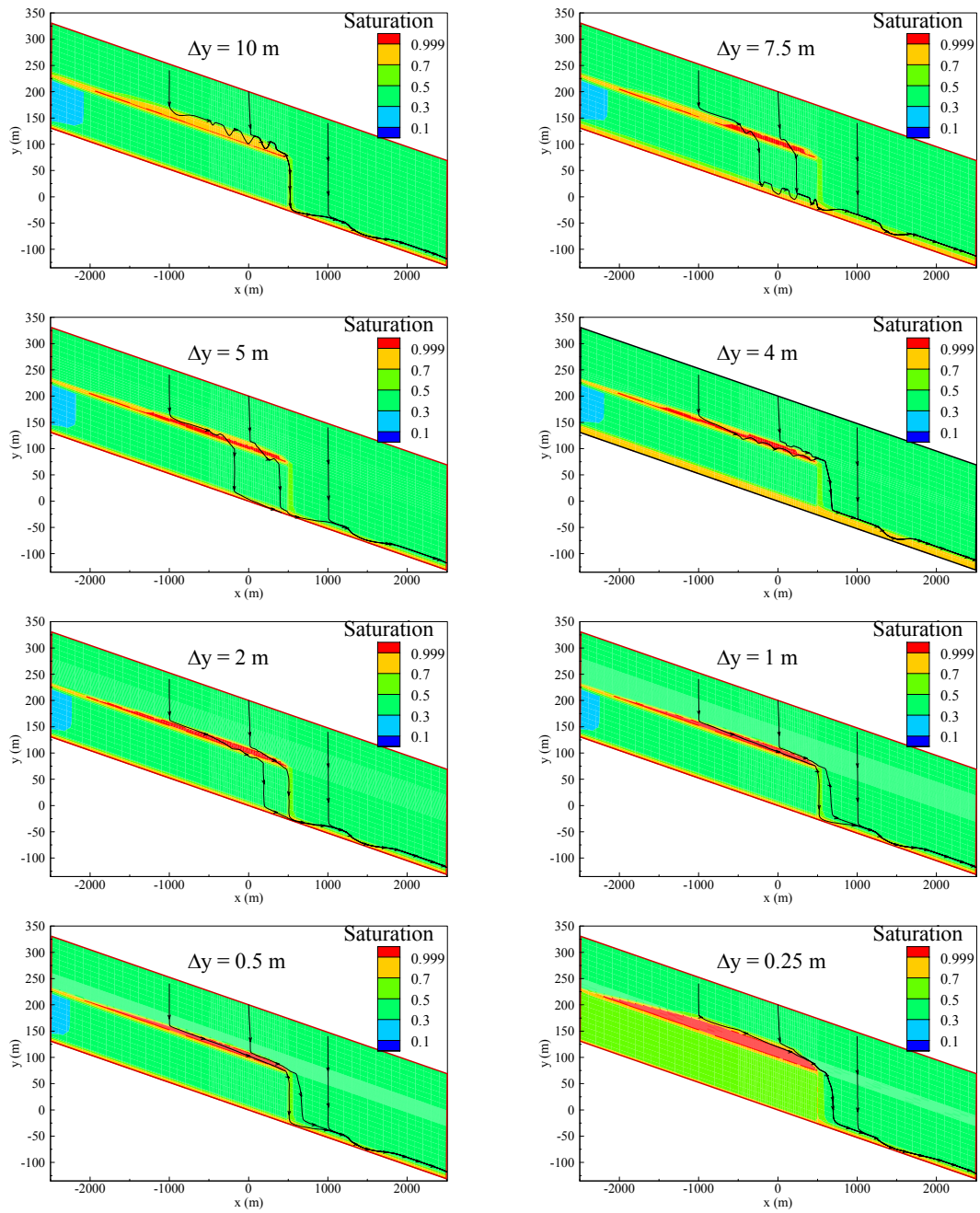


Figure 2.3. Steady-state saturation distribution with different grid resolutions for the base case infiltration rate.

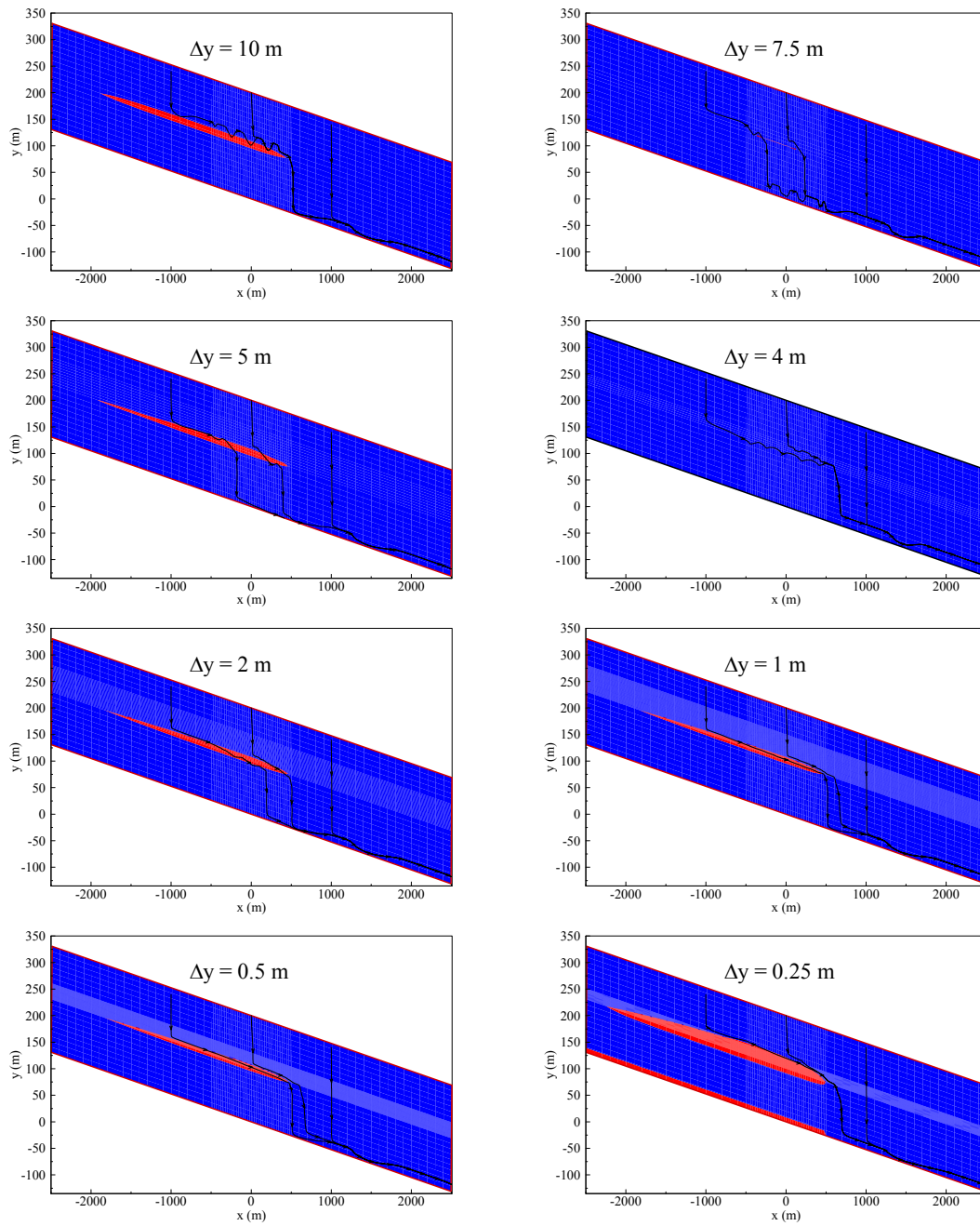


Figure 2.4. Steady-state head distribution for different grid resolutions (red represents positive values) at the base case infiltration rate.

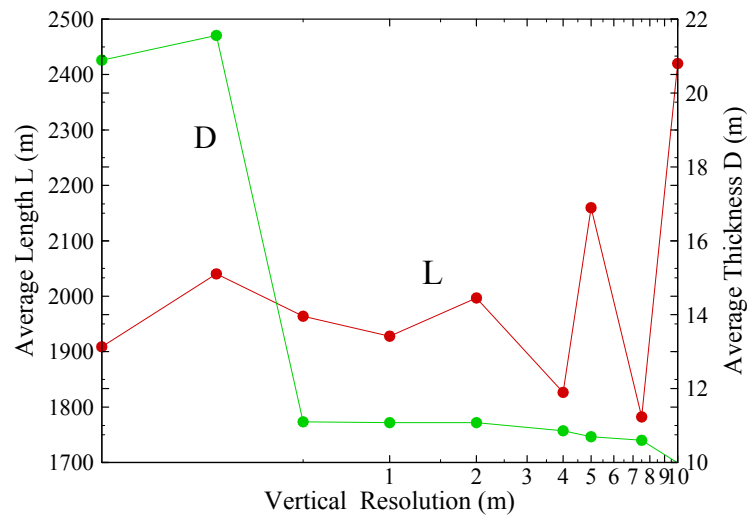


Figure 2.5. The average length and average thickness of perched zone at the final steady state condition for different vertical resolutions for the base case infiltration rate.

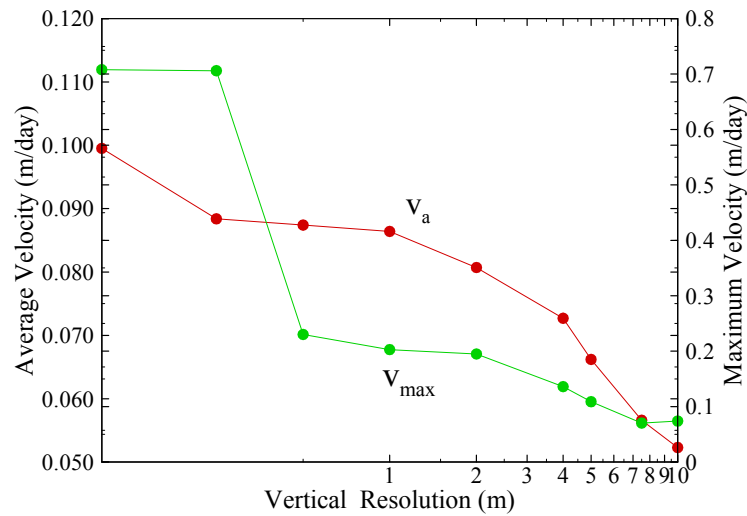


Figure 2.6. Average horizontal velocity component and maximum horizontal velocity in the perched water zone at the final steady state condition for different vertical resolutions for the base case infiltration rate.

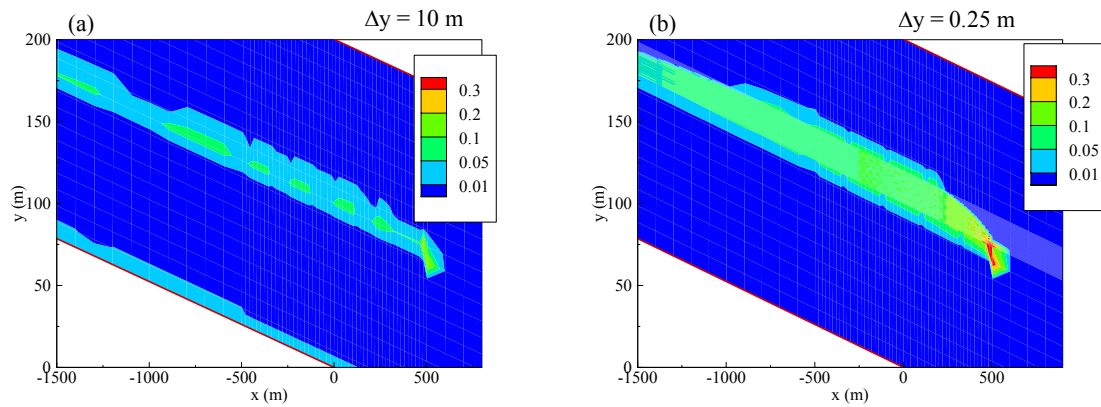


Figure 2.7. The distribution of the horizontal velocity component with vertical resolution of  $\Delta y = 10\text{m}$  and  $0.25\text{m}$  for the base case infiltration rate.

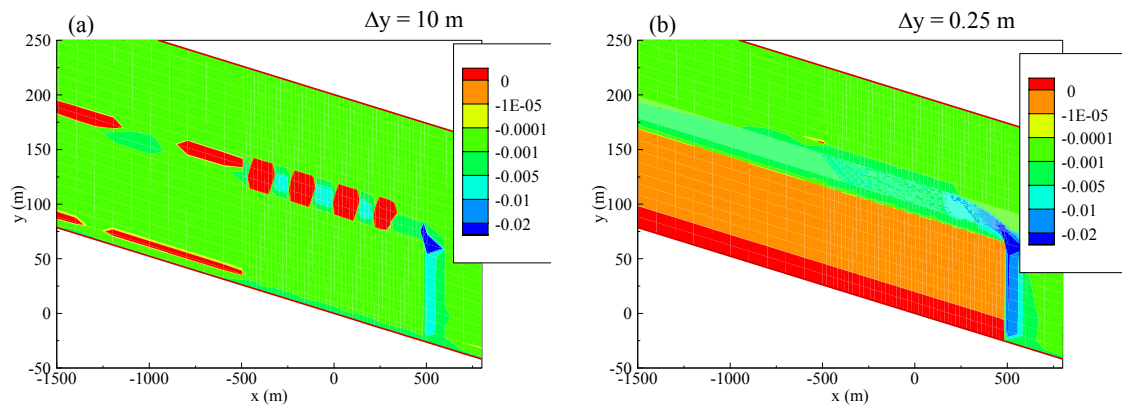


Figure 2.8. The distribution of the vertical velocity component for vertical resolution of  $\Delta y = 10\text{m}$  and  $0.25\text{m}$  for the base case infiltration rate.

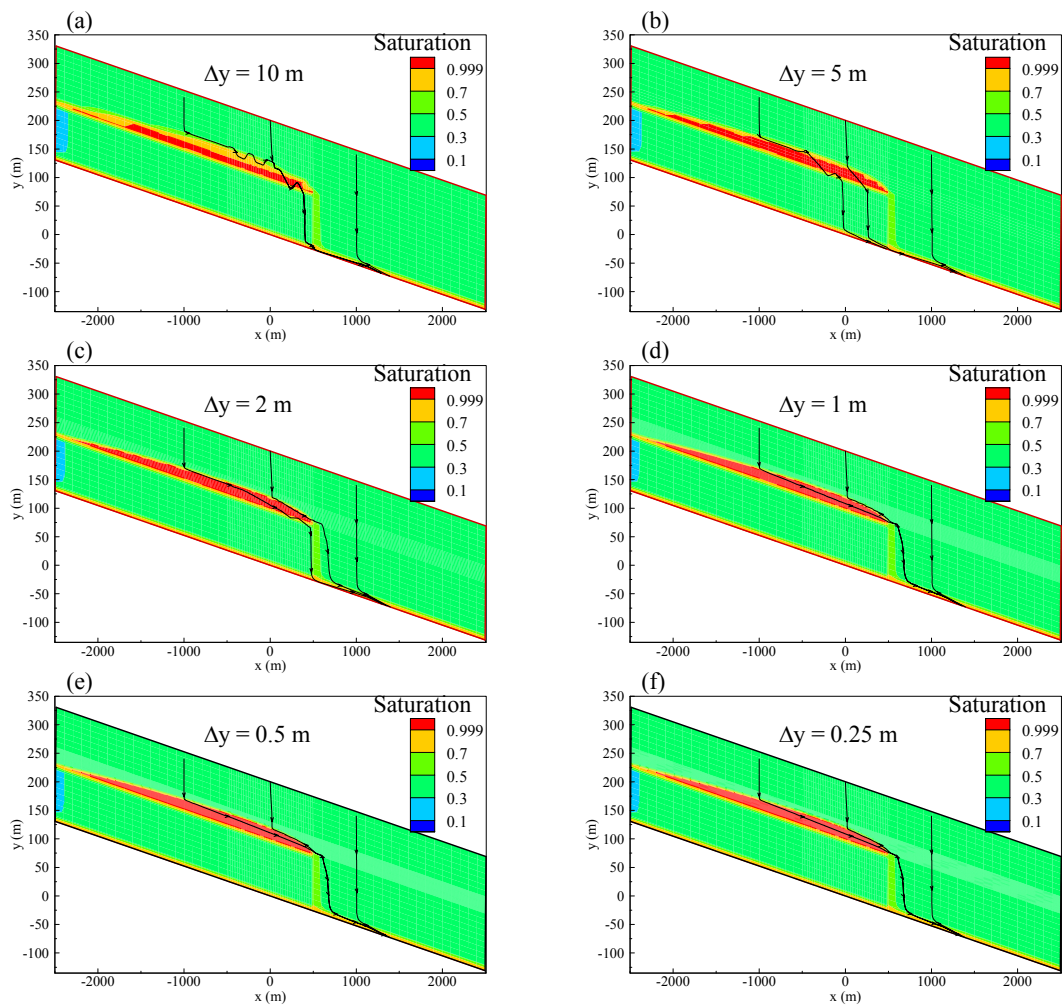


Figure 2.9. Steady-state saturation distribution for different grid resolutions with a higher infiltration rate (250mm/yr).



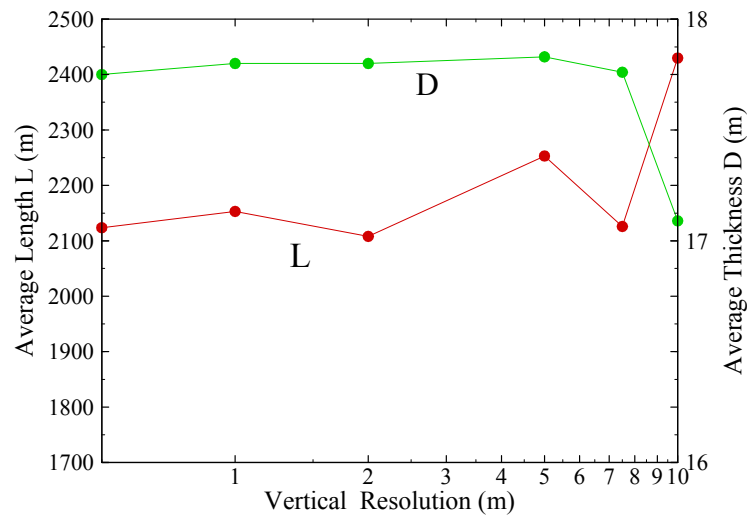


Figure 2.10. The average length and avarage thickness of perched zone at the final steady state condition different vertical resolutions with a higher infiltration rate of 250mm/yr.

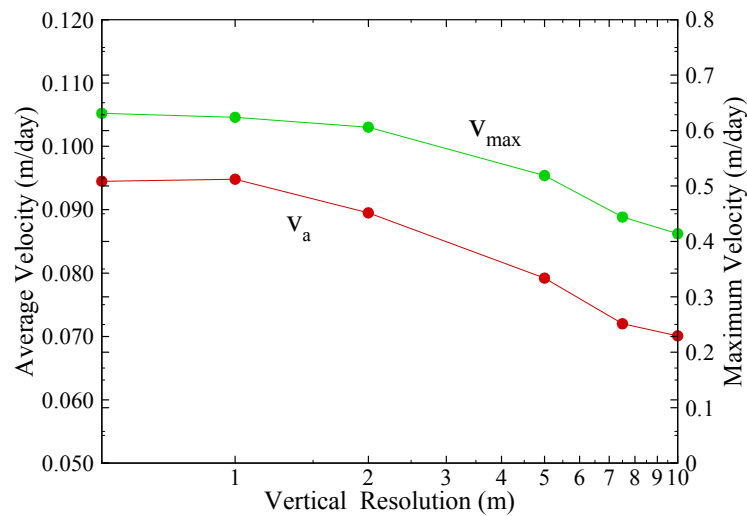


Figure 2.11. Mean velocity and maximum velocity in the perched water zone for different vertical resolutions with a higher infiltration rate of 250mm/yr.

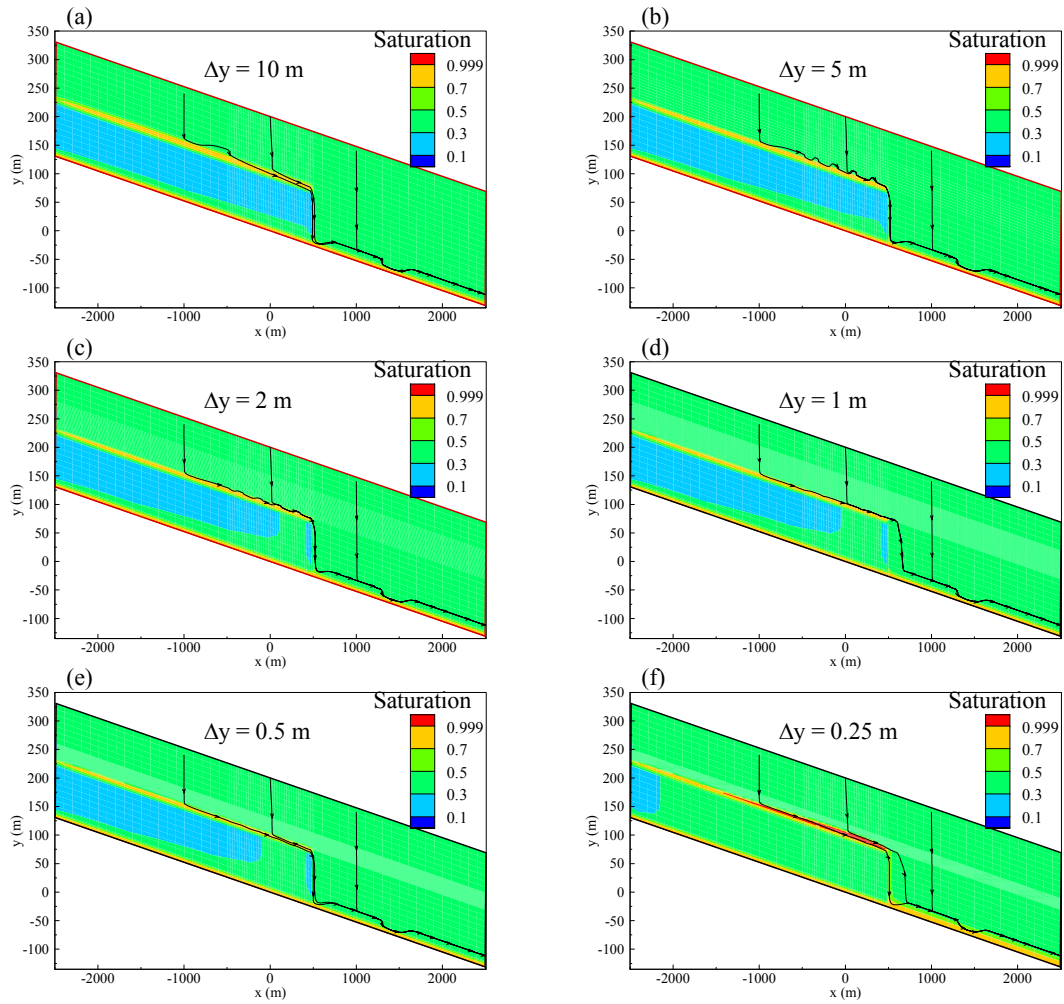


Figure 2.12. Steady-state saturation distribution for different grid resolutions with a lower infiltration rate (50mm/yr).

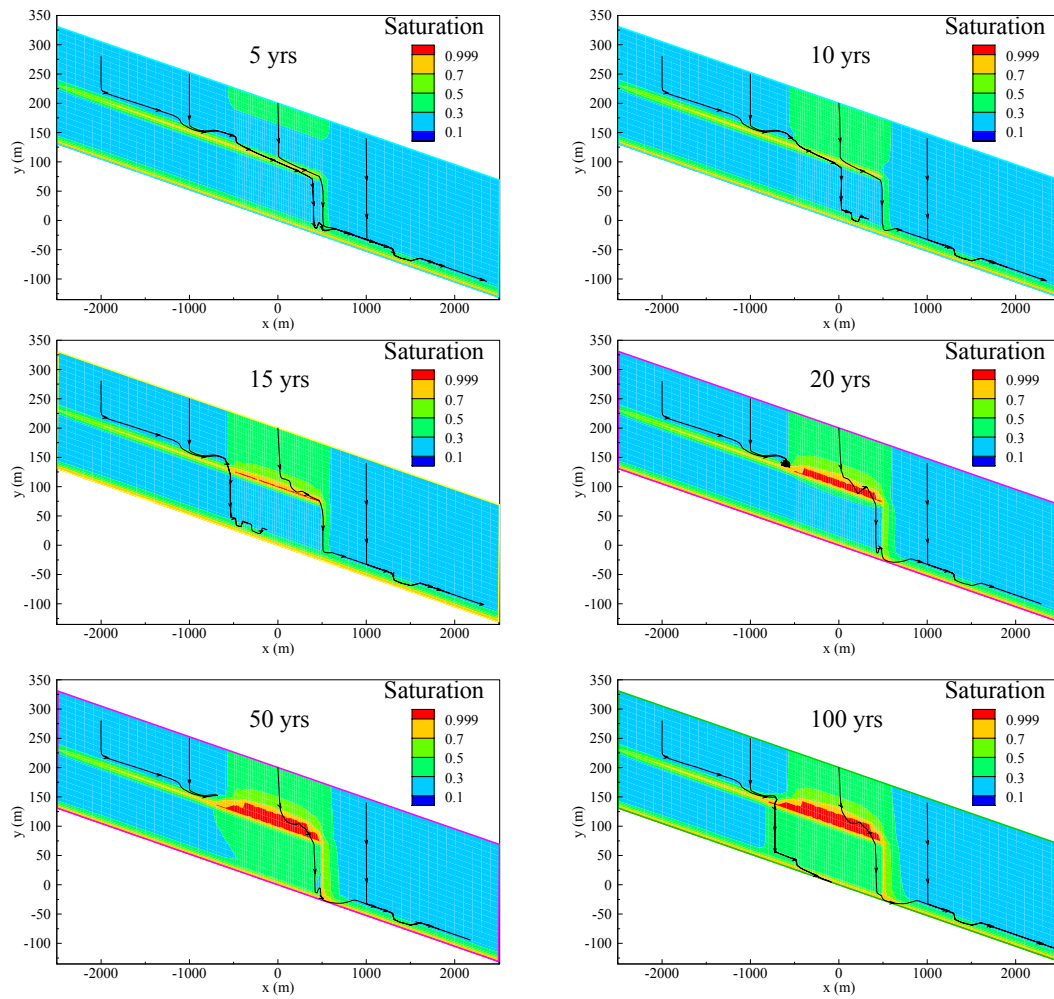


Figure 2.13. Saturation distribution at different elapsed times for the vertical resolution of 10m.

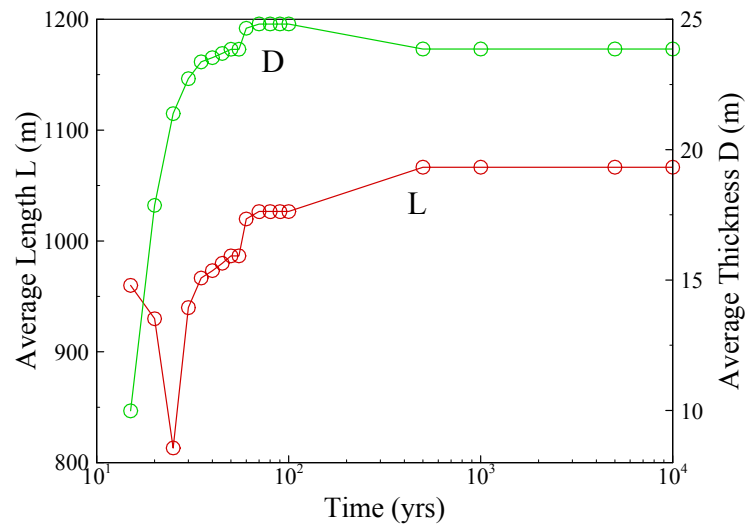


Figure 2.14. The average length and average thickness of perched zone at different elapsed times for the vertical resolution of 10m.

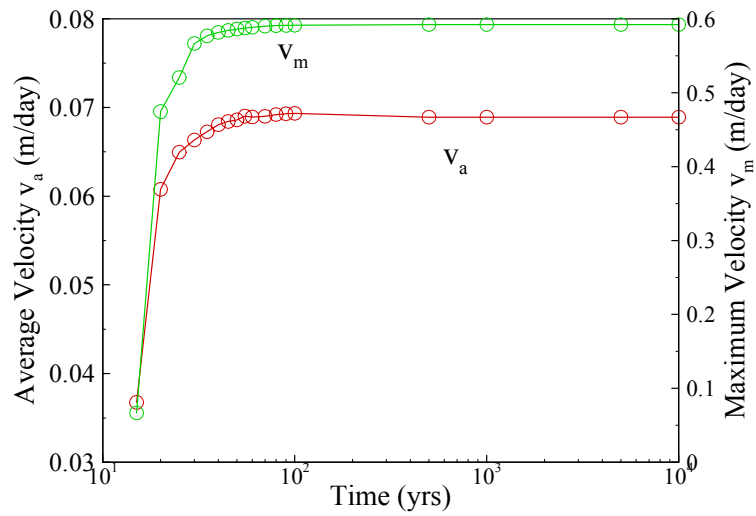


Figure 2.15. Mean velocity and maximum velocity in the perched water zone at different elapsed times for grid resolution of 10m.

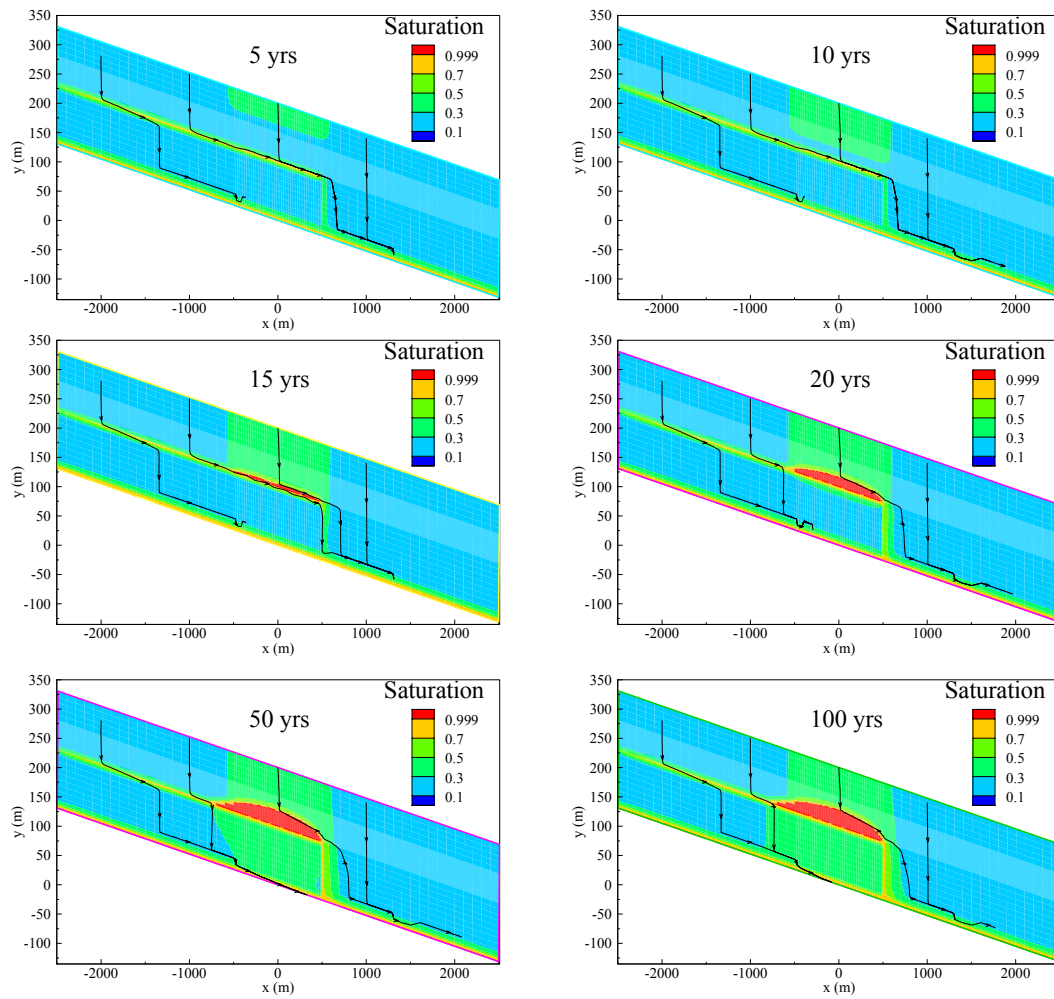


Figure 2.16. Saturation distribution at different elapsed times for the vertical resolution of 1m.

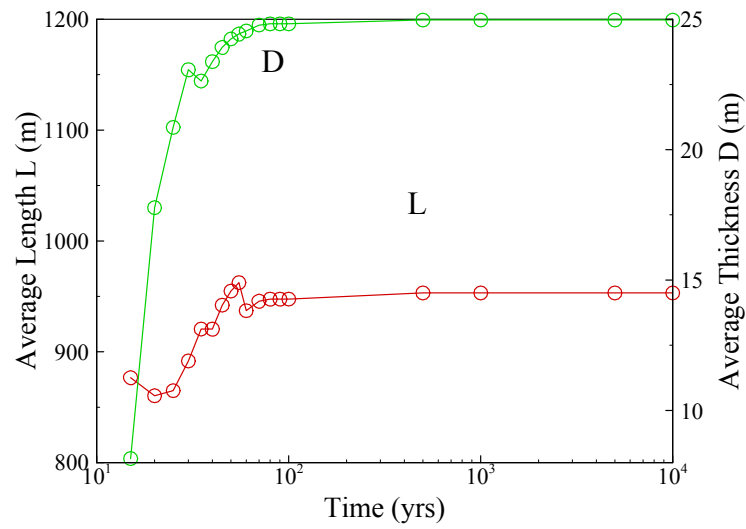


Figure 2.17. The average length and average thickness of perched zone at different elapsed times for the vertical resolution of 1m.

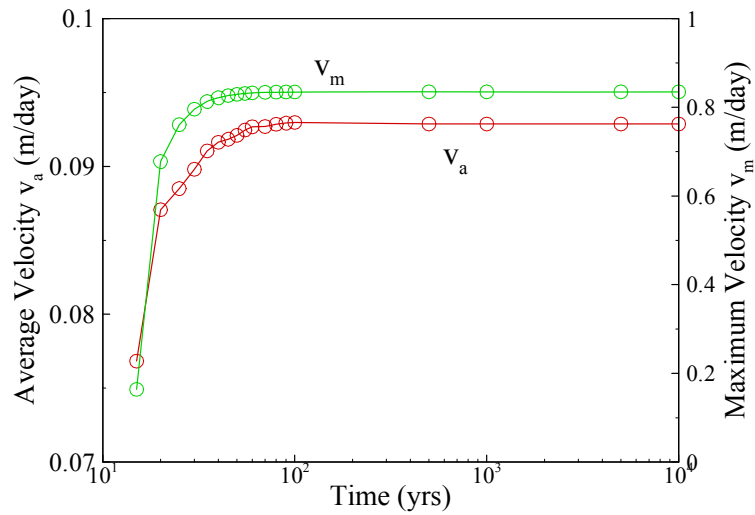


Figure 2.18. Mean velocity and maximum velocity in the perched water zone at different elapsed times for the vertical resolution of 1m.

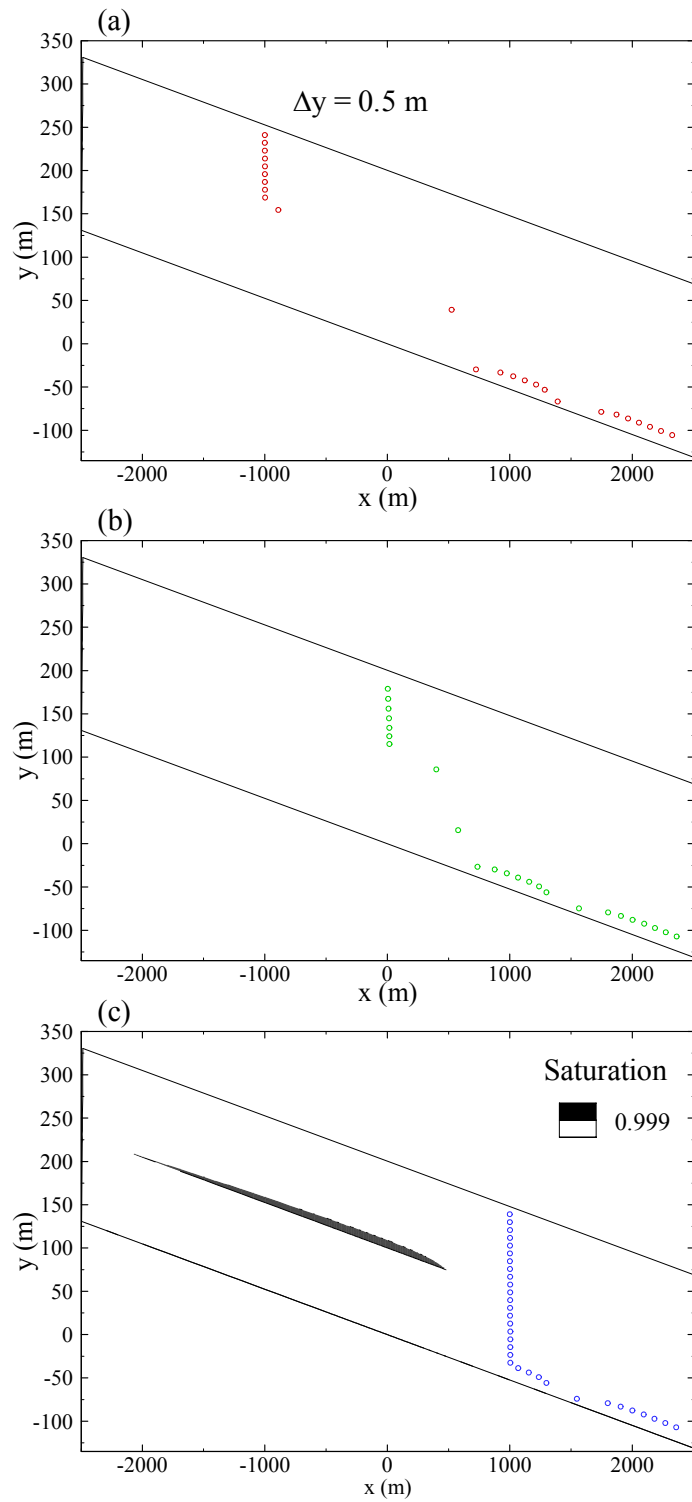


Figure 3.1. The particles' positions at different elapsed times for the base case infiltration rate.

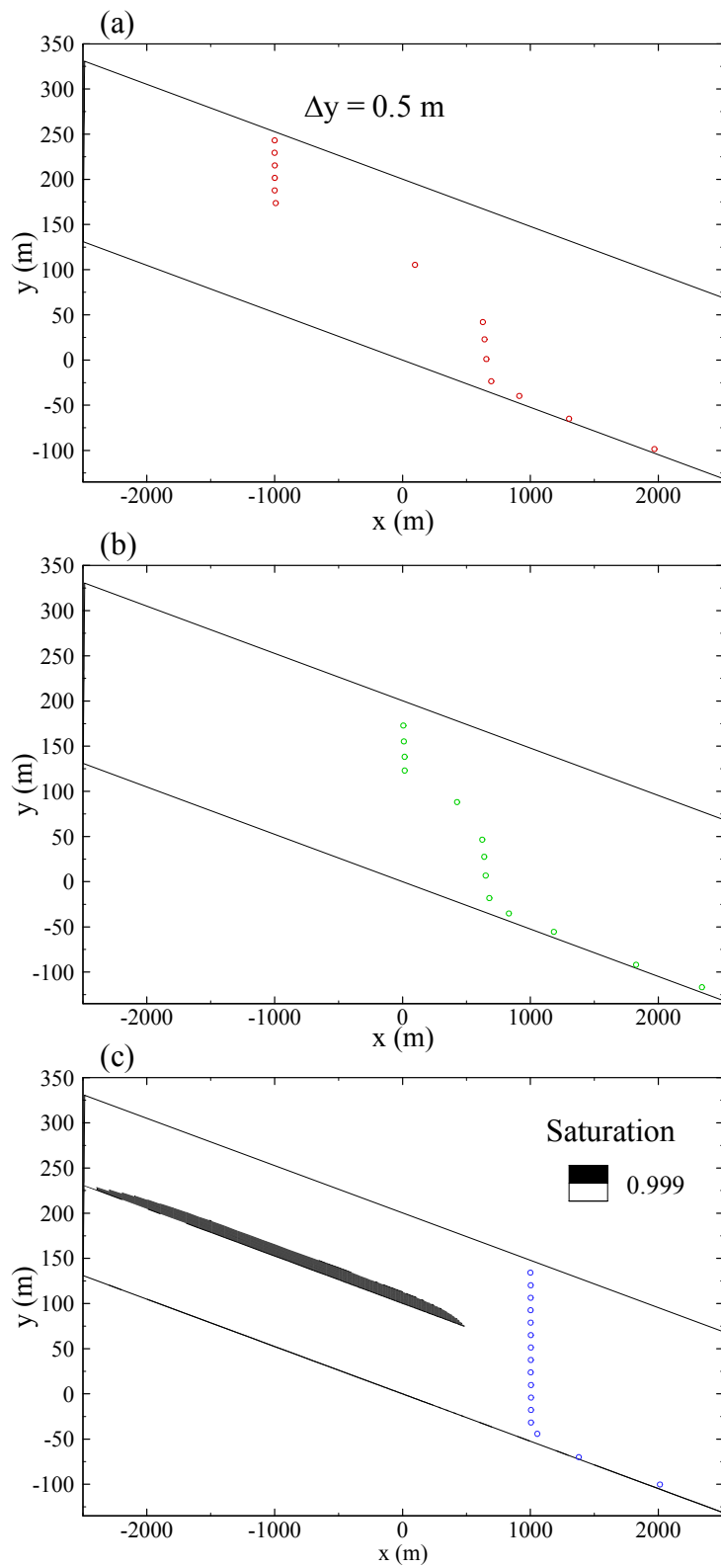


Figure 3.2. The particles' positions at different elapsed times for the higher infiltration rate of 250mm/yr.



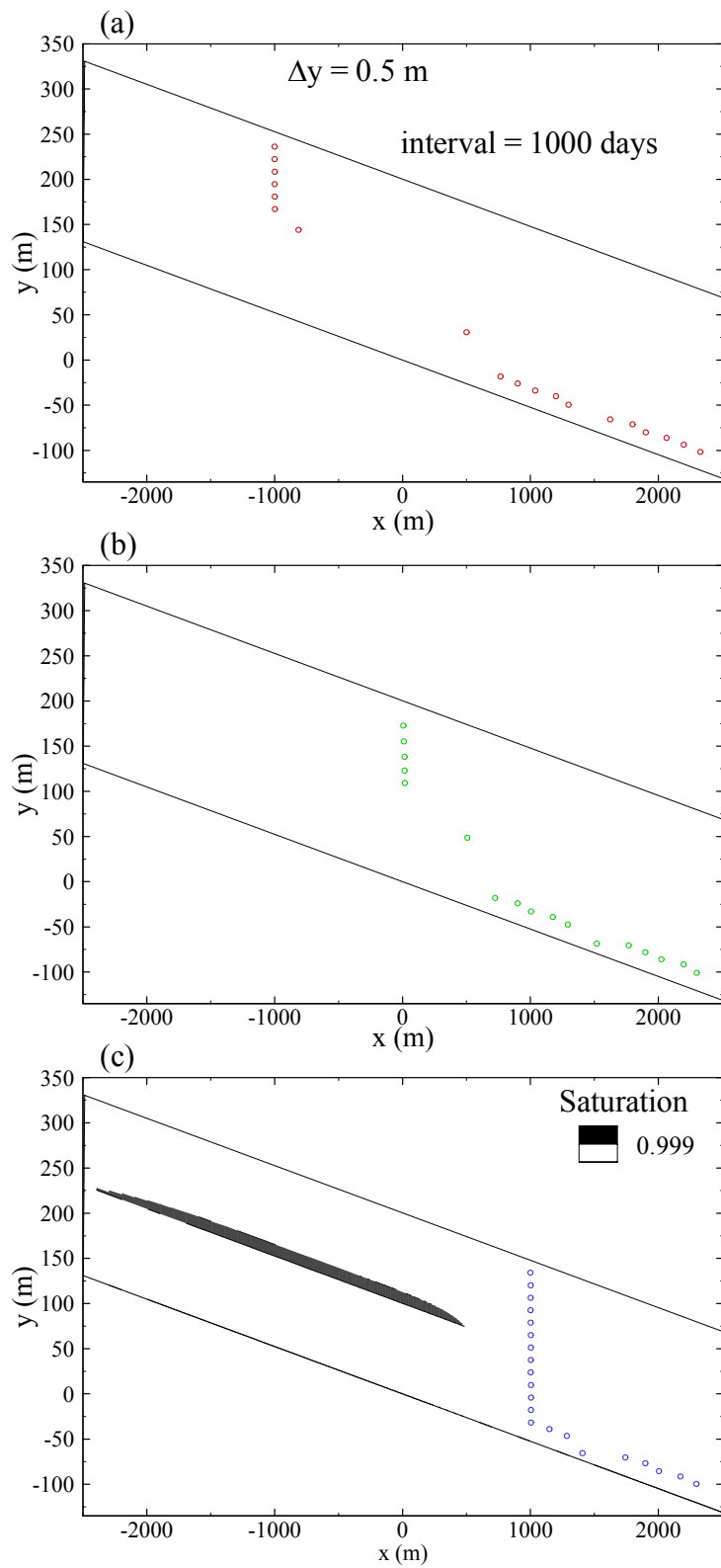


Figure 3.3. The particles' positions at different elapsed times for the lower infiltration rate of 50mm/yr.

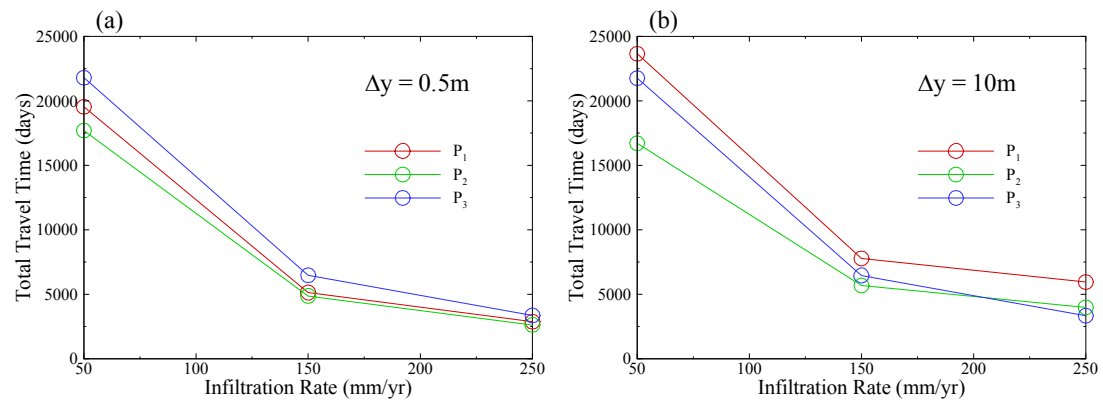


Figure 3.4. The total travel time as a function of the infiltration rate for two vertical grid resolutions.

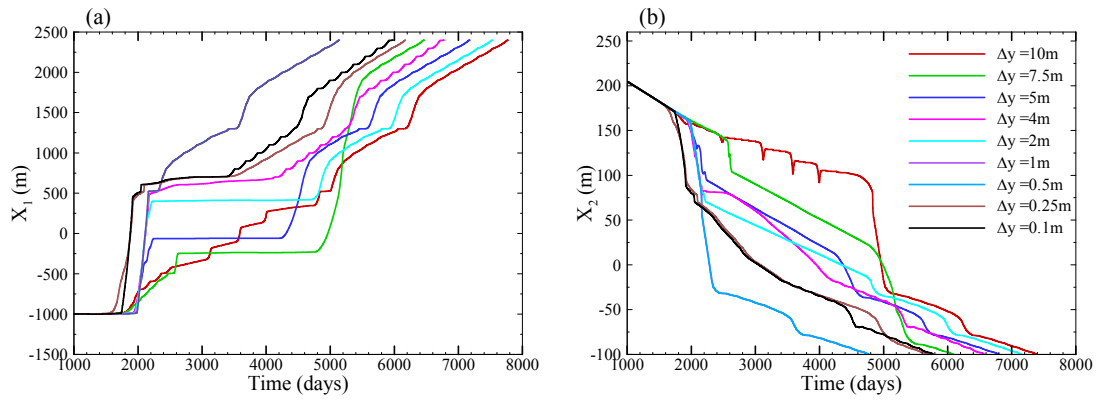


Figure 3.5. Trajectories of particle 1 realised at (-1000m,240m) for different verticle resolution under the net infiltration rate of 150mm/year.

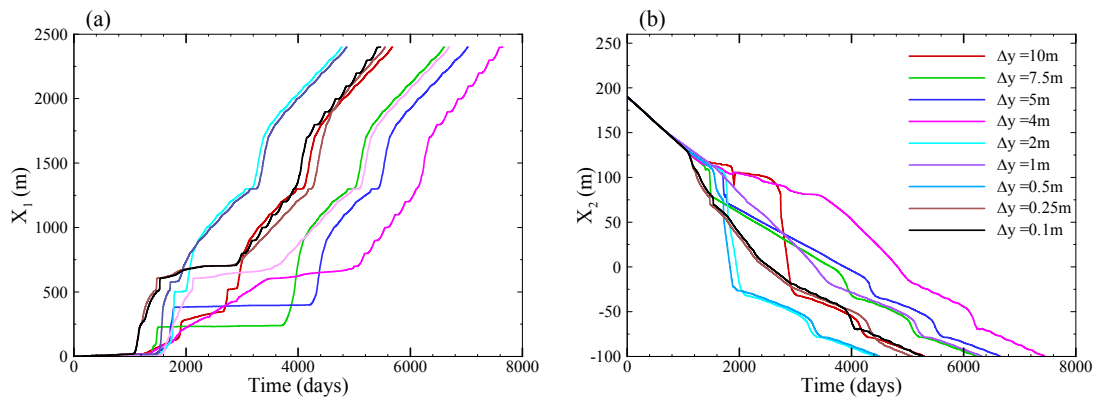


Figure 3.6. Trajectories of particle 2 realised at (0m,180m) for different verticle resolution under the net infiltration rate of 150mm/year.

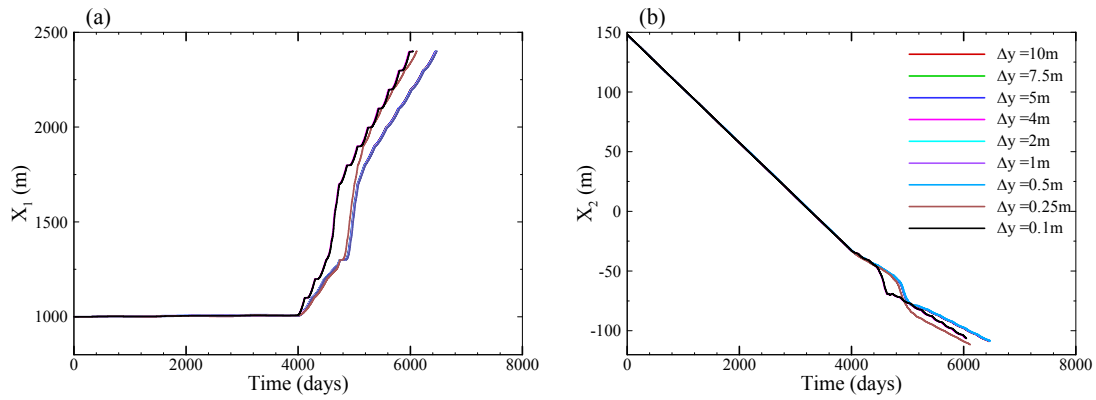


Figure 3.7. Trajectories of particle 3 realised at (1000m,140m) for different vertice resolution under the net infiltration rate of 150mm/year.

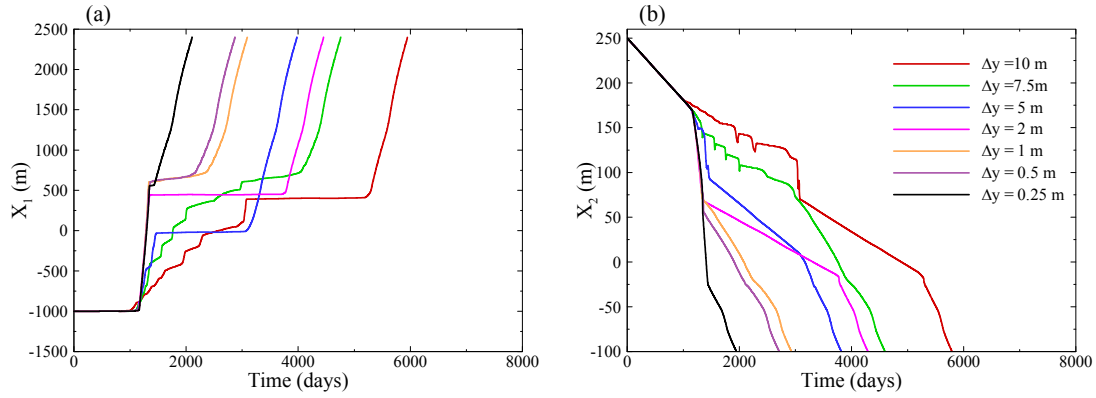


Figure 3.8. Trajectories of particle 1 realised at (-1000m,240m) for different vertice resolution under the net infiltration rate of 250mm/year.

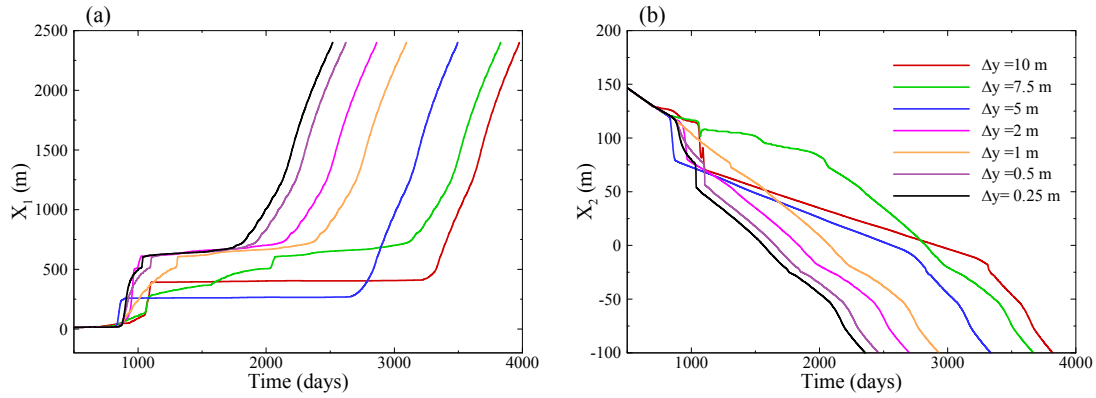


Figure 3.9. Trajectories of particle 2 realised at (0m,180m) for different vertice resolution under the net infiltration rate of 250mm/year.

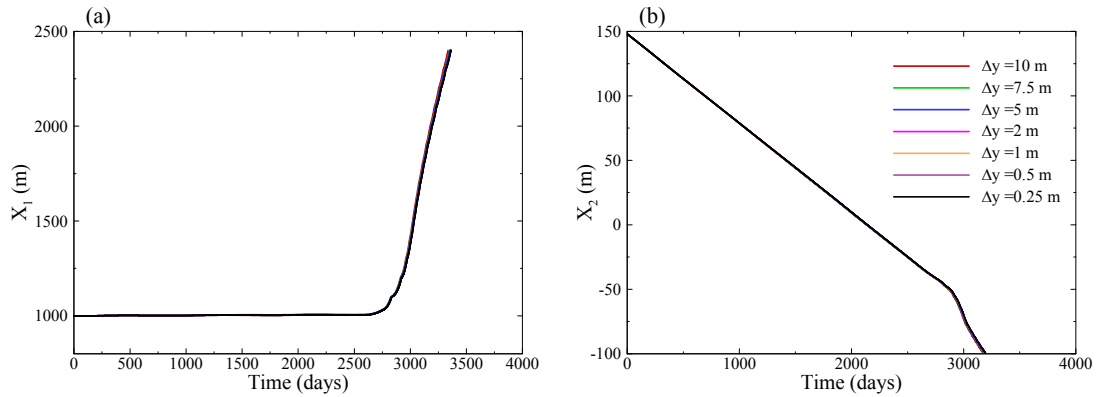


Figure 3.10. Trajectories of particle 3 realised at (1000m,140m) for different vertical resolution under the net infiltration rate of 250mm/year.

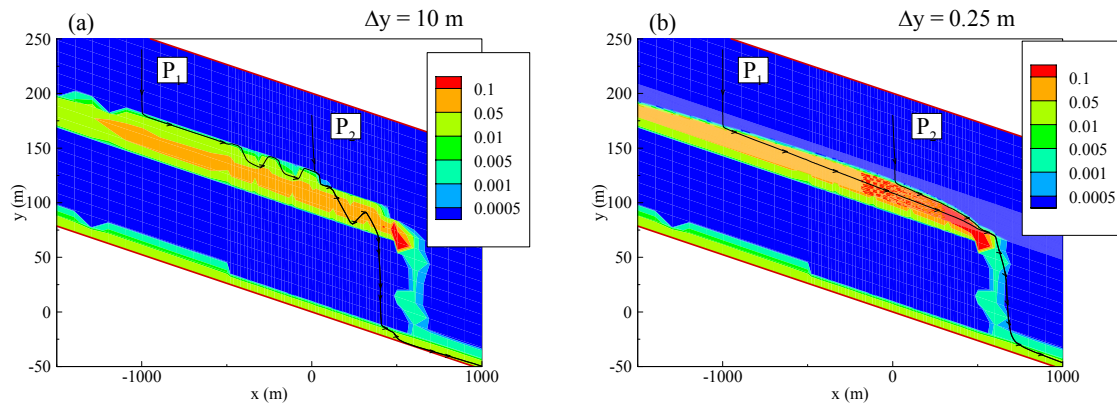


Figure 3.11. The distribution of the horizontal velocity component with vertical resolution of  $\Delta y = 10$ m and 0.25m for the infiltration rate of 250mm/yr.

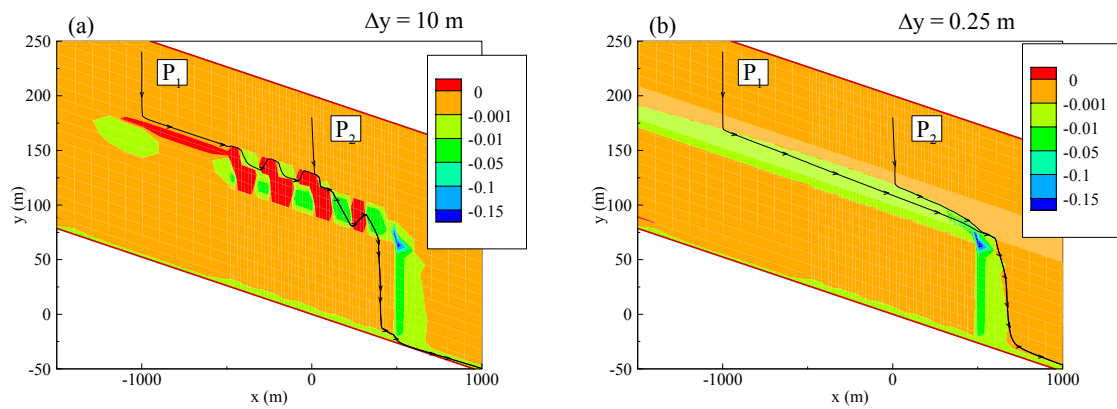


Figure 3.12. The distribution of the vertical velocity component with vertical resolution of  $\Delta y = 10\text{m}$  and  $0.25\text{m}$  for the infiltration rate of  $250\text{mm/yr}$ .

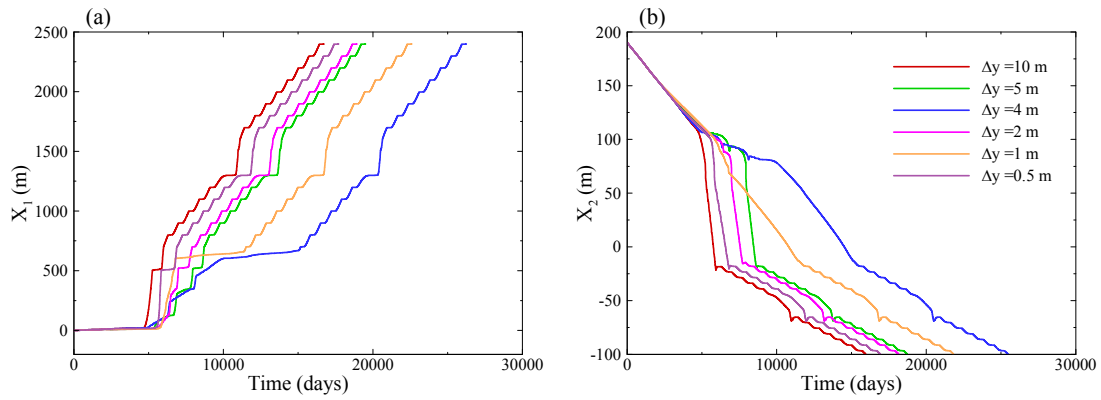


Figure 3.13. Trajectories of particle 1 realised at (-1000m,240m) for different vertical resolution under the net infiltration rate of 50mm/year.

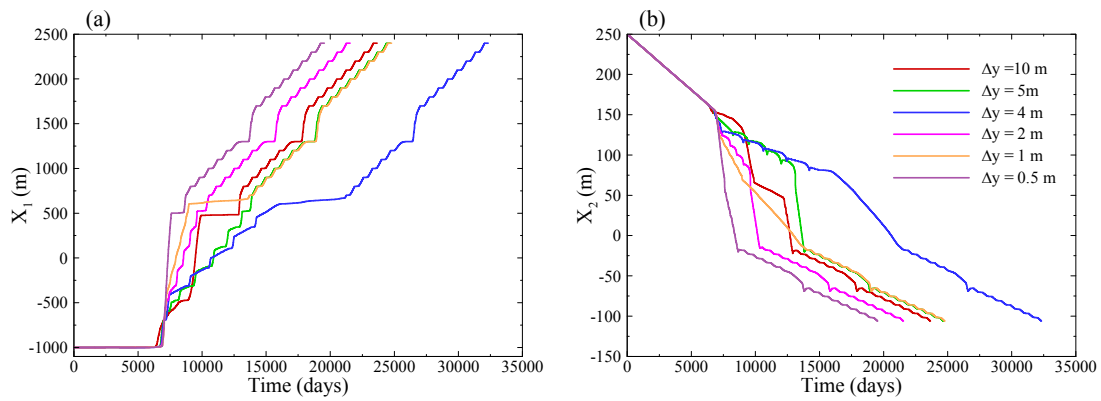


Figure 3.14. Trajectories of particle 2 realised at (0m,180m) for different vertical resolution under the net infiltration rate of 50mm/year.

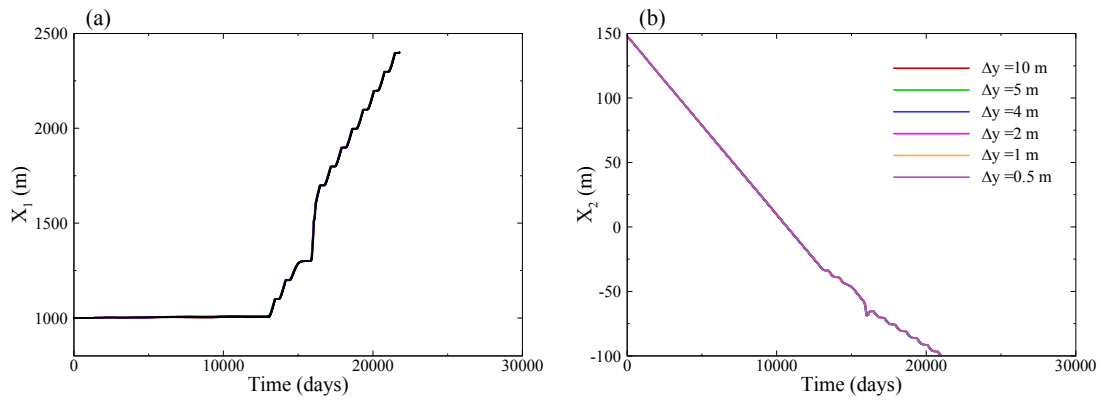


Figure 3.15. Trajectories of particle 3 realised at (1000m,140m) for different verticle resolution under the net infiltration rate of 50mm/year.